CFD-DEM simulations of solid-liquid flow in stirred tanks using a non-inertial frame of reference

Bastien Delacroix[a], Juliane Rastoueix[a], Louis Fradette[a], François Bertrand[a,|], Bruno Blais[a,|]

[a]*Research Unit for Industrial Flows Processes (URPEI), Department of Chemical Engineering, École Polytechnique de Montréal, PO Box 6079, Stn Centre-Ville, Montréal, QC, Canada, H3C 3A7*

Abstract

Mixing applications operating in the laminar regime are used in numerous industrial processes in the pharmaceutical, chemical, and food industries. The aim of this paper is to introduce a numerical model adapted to solid-liquid mixing situations in stirred tanks. The method presented herein is based on a Euler-Lagrange approach using the CFD-DEM method. This method couples computational fluid dynamics (CFD) for the fluid with the discrete element method (DEM) for the solid particles. We introduce a rotating frame of reference approach, which is the first of its kind for CFD-DEM. In this paper we discuss the main issues related to the modeling of complex rotating impeller geometries, we explain the various issues involved in conducting a CFD-DEM simulation in a non-inertial frame, we compare our model with experimental results obtained with a pitched blade turbine and, lastly, we use our model to study solid-liquid mixing with a double helical ribbon.

Keywords: CFD-DEM, Multiphase flows, non-inertial frame, single reference frame, solid-liquid mixing, close-clearance impeller

1. Introduction

Solid-liquid mixing is a versatile and widespread process that is critical to the pharmaceutical, biomechanical, food processing, and other industries. Despite the relevance of viscous solid-liquid mixing applications, the physics governing

*Corresponding authors

Email addresses: francois.bertrand@polymtl.ca (François Bertrand), bruno.blais@polymtl.ca (Bruno Blais)

the viscous suspension of particles in agitated vessels is poorly understood and historically much less studied than in the turbulent regime [7]. This can lead to sub-optimal designs, significant waste of energy, and even an inability to achieve the required mixing state. According to the Handbook of Industrial Mixing [57], when conducting solid-liquid mixing operations it is important to ensure optimal mass transfer between the phases by maximizing the interfacial area. Kneule [42] demonstrated that it is necessary to completely suspend all the particles to achieve this. Based on Zwietering's criterion [80], a particle is considered suspended when it remains in contact with the bottom of the vessel for less than 2s. Zwietering presented the first empirical correlation for the estimation of N_{js}, the speed required to just suspend particles in a mixing system [80]. More than 60 years after its publication, this correlation remains very popular. It is still extensively used in industry despite the fact that it has shortcomings with respect to viscous fluids, high volume fractions, and large particle diameters [8, 38, 48]. For example, the Zwietering correlation predicts an increase of Njs with the particle size and the fluid viscosity whereas Lassaigne et al [45] showed that it is the opposite in the laminar regime. This lead to uncertainties of more than 50% on the determination of Njs. Many attempts have been made to replace this correlation, including those by Nienow *et al.* in 1968 [54], Baldi *et al.* in 1978 [11], Armenante et *al.* in 1998 [6], Ayranci *et al.* in 2013 [9], Tamburini *et al.* in 2014, [66], Grenville *et al.* in 2016 [36], and more recently by Choong *et al.* using an artificial neural network [25]. However, a reliable and universal correlation to predict just suspended speed remains a challenge.

The experimental determination of N_{js} remains difficult. A large number of methods have been developed over the past 50 years. They can be separated into two distinct categories: non-intrusive and intrusive methods. For the first category, the simplest methods are based on direct visual observations [31, 80]. However, they remain limited to transparent vessels and low-concentration systems [56]. Other non-intrusive methods include power number variation analyses [62], and techniques based on light intensity variations [5], radioactive particle tracking [61], pressure measurements (pressure gauge technique) [44, 45, 48], and electrical resistance tomography [15, 45]. Intrusive methods are relatively problematic because they disrupt the flow [35] by measuring particle concentrations at different locations directly in the vessel using sampling or physical measurements (e.g. conductivity) [22].

Lastly, computer simulations are another way to approach the problem. This will be the subject of this paper. We begin with a brief review of existing

approaches and the various issues involved in modeling viscous solid-fluid flows.

1.1. Modeling solid-fluid interactions

It is important to note that the accuracy and the computational cost of numerical models used are greatly influenced by the scale at which the interactions are simulated. Three different scales can be defined: the macroscopic scale, which corresponds to the characteristic dimensions of the system, the microscopic scale, which is the particle scale, and, lastly, the mesoscopic scale, which corresponds to the size of coherent structures within the flow [55, 76]. For multiphase systems each phase can be solved with its own scale. Three main approaches for studying solid-liquid mixing applications are summarized in Figure 1: the two-fluid model, the resolved CFD-DEM, and the unresolved CFD-DEM.

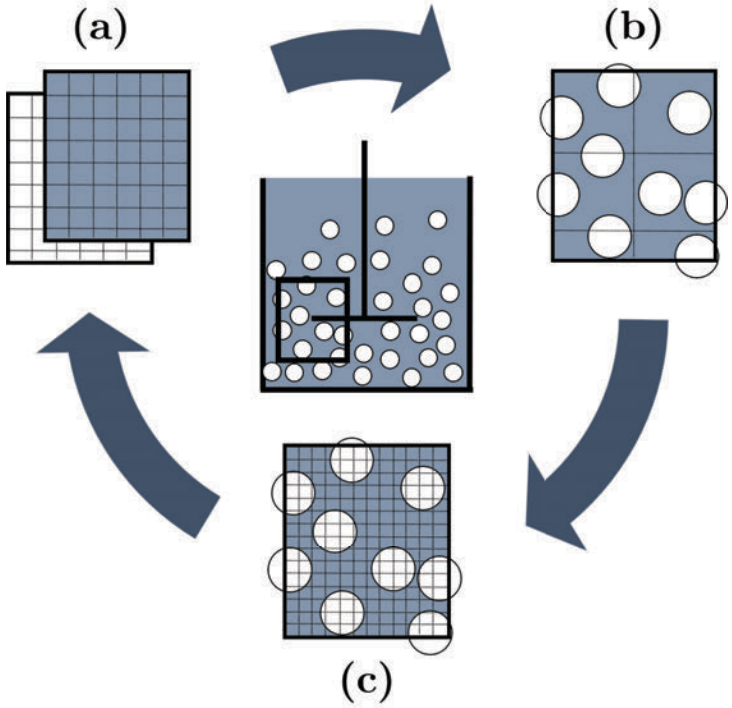

Figure 1: Representation of the various scales involved in a solid-liquid mixing system: (a) meso-meso scale with the two-fluid model, (b) meso-micro scale with unresolved CFD-DEM, and (c) meso-micro scale with resolved CFD-DEM.

1.1.1. Euler-Euler approach

The Euler-Euler approach is a meso-meso scale strategy. It generally uses the two-fluid model in which the solid and liquid phases are treated as interpenetrating continua. This saves calculation time, which explains why the majority of numerical studies on solid-liquid mixing have been carried out with this approach. Micale et *al.* [49] showed that this model can predict the cloud height, which is defined as the distance from the bottom of the vessel to the level where the majority of the particles are lifted [57]. Likewise, Tamburini et *al.* made a significant contribution to the numerical analysis of solid-liquid mixing operations with the two-fluid model in a series of articles [4, 67, 68, 69, 70, 72]. They showed that the two-fluid model can predict the impact of different physical and geometrical parameters, on the quality of the mixing. However, considering the solid phase as a single continuous entity results in the loss of a considerable amount of information on granular dynamics, which can be problematic for determining the distribution of particles in a mixing tank and thus estimating important parameters such as N_{js} [67].

1.1.2. Euler-Lagrange approach

An alternative solution is to use a microscopic approach to study particles while resolving the fluid with a different scale. The main advantage of the Euler-Lagrange approach is that it takes the motion of each particle into consideration. However, this type of approach remains marginal in the study of solid-liquid mixing systems due mainly to the computational cost, which is greatly affected by the number of particles. One of the most interesting methods based on this approach is CFD-DEM, which combines CFD for fluid mechanics and the discrete element method (DEM) for granular dynamics. There are two categories of CFD-DEM [14]. The first is called resolved CFD-DEM and is characterized by a fluid mesh cell smaller than the particle diameter. This method can accurately reproduce the different hydrodynamic phenomena. However, the modeling is generally limited to a small number of particles ($< 10^4$ [29]). An alternative strategy is unresolved CFD-DEM where the fluid mesh cell size is larger than the particle diameter. This makes it possible to increase the number of particles while maintaining good accuracy. This method was used by [74] with Rushton turbines and by [17, 18, 19] with pitched blade turbines.

For more details about the different numerical methods used to model solid-liquid mixing we refer to the review by Mishra et *al.* [51].

1.2. Boundary conditions in motion: strategy and issues

One of the most important issues in modeling a mixing operation is the rotation of the impeller. This section will provide a brief description of the various methods used to deal with this issues. For more details about these methods we refer to the reviews by Brucato *et al.* [23] and Blais *et al.* [20].

1.2.1. Multiple reference frame method

Multiple reference frames deal with the rotation of the impeller by decomposing the domain into two different frames: the Lagrangian frame in rotation, which contains the rotating geometry, and the Eulerian frame of reference, which encompasses the stator (the vessel and baffles). The Navier-Stokes (NS) equations are solved with the specific component of the acceleration for each sub-domain. The main constraint of this method is that it is limited to steady-state simulations to ensure good coupling at the mesh interface between the two sub-domains [47]. As solid-liquid mixing is inherently transient the multiple reference frame approach cannot be used in such a case.

1.2.2. Sliding mesh method

The sliding mesh approach is one of the most commonly used for unsteady-state studies of solid-liquid mixing systems [49, 52, 68, 69, 70].This approach decomposes the system into two non-overlapping regions, one with a fixed grid with the tank and one or more moving grids that contain the rotating components (e.g., the impeller). In the static region, fluid motion resolution is based on the classical NS equations. In the other region, additional terms are introduced in the NS equations to take into account the difference in velocity between the fluid and the rotating grid. These two regions are coupled by an interpolation of the information at their interface to ensure the conservation of the flux. This model is relatively reliable for solid-liquid mixing modeling compared with the MRF method [53]. The main constraints of this method are that it is relatively computationally expensive and that it is challenging to handle small gaps between the rotor and the stator to ensure the accuracy of the interpolation [51].

1.2.3. Immersed boundary method

The particularity of this method is that it does not require a body fitted mesh of the geometry. There are two core approaches for the immersed boundary model: the discrete and the continuous. In the discrete approach, the flow is

modified after the integration of the classical NS equations to take the motion of the geometry into account [32, 58, 59]. The continuous approach, which is used in the PISO-IB solver developed by Blais et *al.* [20] in the CFDEM framework [2], imposes the rigid motion of the body by inserting a forcing term directly in the NS equations. For this method, significant local mesh refinement is required over the volume swept by the impeller, which can lead to a considerable number of cells and thus high computational costs.

1.2.4. Single rotating frame method (SRF)

The SRF method completely redefines the problem from the Eulerian frame to the Lagrangian frame linked to the rotating geometry. This requires imposing a no-slip boundary condition on the impeller and a rotating condition on the tank wall. As a rotating frame is not a Galilean frame the Coriolis and centrifugal forces have to be taken into account in the equations for the momentum conservation (1).

$$\frac{\partial \rho_f \mathbf{u}_f}{\partial t} + \nabla(\rho_f \mathbf{u}_f \leq \mathbf{u}_f) = -\nabla p + \nabla \cdot \boldsymbol{\tau} + \rho_f \mathbf{g} \underbrace{2\rho_f \boldsymbol{\Omega} \otimes \boldsymbol{u}_f}_{Coriolis} \underbrace{\rho_f \boldsymbol{\Omega} \otimes (\boldsymbol{\Omega} \otimes \boldsymbol{q}_f)}_{Centrifugal} \tag{1}$$

where $\boldsymbol{\Omega}$ is the rotation vector of the frame of reference, and $\boldsymbol{q}_f$ and $\boldsymbol{u}_f$ are the position (from the projection point on the axis of rotation: $\boldsymbol{q}_f \cdot \boldsymbol{\Omega} = 0$) and velocity vectors of a fluid cell, respectively.

It is important to note that the SRF method is limited to cases where the stator is symmetrical. It cannot thus be used in systems with baffles, for example. However, baffles are rarely used in the laminar regime as they lead to the formation of dead zones.

1.3. Specificities of viscous solid-liquid mixing

After a brief introduction to the different methods for dealing with the rotation of the impeller and the modeling of solid-fluid systems, we will shed light on the impact of the complexity of the geometry on these different methods. In the laminar regime, it is common to use complex agitators such as the helical ribbon [10, 27]. The parameters used to characterize the complexity of an agitator are shown in Figure 2, which illustrates the main differences between a simple impeller geometry like the pitched blade turbine (PBT) and a more complex geometry like the double helical ribbon (DHR). Three characteristic elements emerge from this comparison:

– The volume swept by the impeller (V_s).

– The distance to the wall (E).

– The characteristic dimension of an element of the impeller, such as the thickness of a ribbon (e), which can be very small.

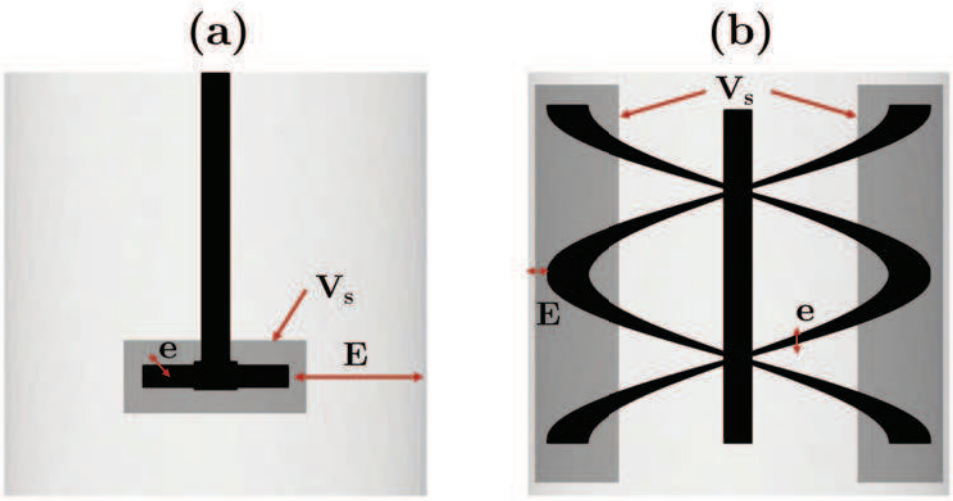

Figure 2: Illustration of the differences in geometry of: (a) a relatively simple impeller geometry with the PBT and (b) a relatively complex impeller geometry with the DHR.

In the previous section we discussed the main constraints of the different methods that deal with boundaries in motion. Table 1 summarizes how the three geometrical characteristics of complex impellers are particularly problematic for the application of these methods.

Lastly, based on the observations described above, we chose to develop an unresolved CFD-DEM model in a rotating frame of reference to meet all the requirements of viscous solid-liquid mixing simulations. The model was developed based on our previous assessment of the feasibility of performing DEM in a rotating frame of reference [28]. To the best of our knowledge, only one

	Large swept volume	Close clearance impeller	Small thickness
Immersed boundary	Multiplication of the number of cells	—	Refinement to detect the rotating geometry
Sliding mesh	Large contact area between the two sub-domains	Interpolation inaccuracy	—
Single rotating frame	—	—	—

Table 1: Summary of the main impacts of the different geometrical characteristics of a complex impeller on the numerical methods that deal with boundary conditions in motion.

previous study has dealt with the coupling of CFD and DEM methods in a rotating frame of reference [64] and was limited to the markedly different context of gas-solid flows.

This paper is divided into four parts. The first provides a detailed description of the CFD-DEM model in a rotating frame of reference. The second discusses the feasibility of using CFD-DEM in non-inertial frames based on several test cases. The third is devoted to a comparison of the model with experimental results obtained for an agitated system with a pitched blade turbine. The last part focuses on solid-liquid mixing with a more complex geometry, i.e., the double helical ribbon.

2. Model description

The unresolved CFD-DEM approach proposed in the present study is a combination of two different methods to deal with fluid and solid motion. It is based on the CFDEM framework [2], which combines the open source sofware OpenFOAM [3] for fluid motion and LIGGGHTS [1] for particle motion. Fluid resolution is based on a cell-centered finite volume approach, and particle motion is based on DEM. This part is devoted to a brief description and formulation of these two methods in the context of a rotating frame of reference. Coupling the two methods will then be discussed. Lastly, a summary of the different steps required to set up a CFD-DEM experiment in a non-inertial frame of reference is presented.

2.1. Equations of motion for the solid phase - Discrete Element Method (DEM)

DEM is a Lagrangian approach for modeling granular flows where each particle is considered as a discrete entity. The method integrates Newton's second law of motion to calculate the velocity and position of each particle at every time step of the simulation.

The method specifically deals with collisions by allowing particles to overlap. They are detected by comparing the distance of two particles to the sum of

their radii. If two particles overlap, a simple spring and dashpot model is used to compute a contact force that is decomposed into elastic and dissipative components. Each of these components is divided into a tangential and a normal term.

Based on Newton's second law of motion, the governing equations for the translational ($\boldsymbol{u}_{p,i}$) and rotational ($\boldsymbol{\omega}_{p,i}$) motions of particle i in a non-inertial frame of reference can be written as [1, 21, 79]:

$$m_i \frac{d\boldsymbol{u}_{p,i}}{dt} = \sum_j \boldsymbol{f}_{c,ij} + \sum_k \boldsymbol{f}_{lr,ik} + \boldsymbol{f}_{pf,i} + \boldsymbol{f}_{g,i} \quad \underbrace{2m_i \boldsymbol{\Omega} \otimes \boldsymbol{u}_{p,i}}_{Coriolis} \quad \underbrace{m_i \boldsymbol{\Omega} \otimes (\boldsymbol{\Omega} \otimes \boldsymbol{q}_{p,i})}_{Centrigugal} \tag{2}$$

$$I_i \frac{d\boldsymbol{\omega}_{p,i}}{dt} = \sum_j (\boldsymbol{M}_{t,ij} + \boldsymbol{M}_{r,ij}) \quad \underbrace{I_i(\boldsymbol{\Omega} \otimes \boldsymbol{\omega}_{p,i})}_{Coriolis} \tag{3}$$

where m_i is the mass of particle i, $\boldsymbol{\Omega}$ is the rotation vector of the frame of reference, $\boldsymbol{q}_{p,i}$ and $\boldsymbol{u}_{p,i}$ are the position (from the projection point on the axis of rotation: $\boldsymbol{q}_{p,i} \times \boldsymbol{\Omega} = 0$) and velocity vectors of a particle i, I_i is the moment of inertia of particle i, $\boldsymbol{\omega}_{p,i}$ is the angular velocity of particle i, $\boldsymbol{f}_{c,ij}$ is the contact forces between particles i and j, $\boldsymbol{f}_{lr,ik}$ is the non-contact (long-range) forces between particles i and k, $\boldsymbol{f}_{pf,i}$ is the particle-fluid interaction forces, $\boldsymbol{f}_{g,i}$ is the gravitational force ($\boldsymbol{f}_{g,i} = m_i \boldsymbol{g}$), and $\boldsymbol{M}_{t,ij}$ and $\boldsymbol{M}_{r,ij}$ are the tangential and rolling friction torques acting on particle i due to its contact with particle j.

In the present work, non-contact forces such as electrostatic or Van Der Waals forces in (2) and the Coriolis torque in (3) were not taken into account due to the size and nature of the particles [28].

The contact forces between two particles are split into normal ($\boldsymbol{f}_{cn,ij}$) and tangential ($\boldsymbol{f}_{ct,ij}$) [78] components:

$$\boldsymbol{f}_{c,ij} = \boldsymbol{f}_{cn,ij} + \boldsymbol{f}_{ct,ij} = \quad k_{n,ij}\boldsymbol{\delta}_{n,ij} \quad \gamma_{n,ij}\dot{\boldsymbol{\delta}}_{n,ij} \quad k_{t,ij}\boldsymbol{\delta}_{t,ij} \quad \gamma_{t,ij}\dot{\boldsymbol{\delta}}_{t,ij} \qquad (4)$$

where $k_{n,ij}$ and $k_{t,ij}$ are the normal and tangential stiffness coefficients, $\gamma_{n,ij}$ and $\gamma_{t,ij}$ are the normal and tangential damping coefficients, $\boldsymbol{\delta}_{n,ij}$ and $\boldsymbol{\delta}_{t,ij}$ are the normal and tangential overlaps, and $\dot{\boldsymbol{\delta}}_{n,ij}$ and $\dot{\boldsymbol{\delta}}_{t,ij}$ are their derivatives with respect to time.

In the present work, we used a model proposed by Tsuji *et al.* [75] based on the Hertz theory [40] for the normal forces. We used the Mindlin model [50] for the tangential forces. These models were combined to couple the stiffness and damping coefficients to Young's modulus of the material (Y), Poisson's ratio (ν), and the coefficient of restitution (e_r) using the equations given in Table 2. The tangential overlap $\boldsymbol{\delta}_{t,ij}$ was truncated using Coulomb's law to ensure that:

$$\boldsymbol{f}_{ct,ij} \mid \quad \mu_{s,ij} \sqrt{\boldsymbol{f}_{cn,ij}} \frac{\boldsymbol{\delta}_{t,ij}}{\sqrt{\boldsymbol{\delta}_{t,ij}}\nabla}$$

Parameter	Equation
Normal stiffness	$k_{n,ij} = \frac{4}{3} Y_{ij}^{\vert} \sqrt{R_{ij}^{\vert} \delta_{n,ij}}$
Tangential stiffness	$k_{t,ij} = 8 G_{ij}^{\vert} \sqrt{R_{ij}^{\vert} \delta_{n,ij}}$
Normal damping	$\gamma_{n,ij} = 2 \sqrt{\frac{5}{6}} \nabla \frac{\ln(e_r)}{\sqrt{\ln^2(e_r) + \pi^2}} \sqrt{\frac{2}{3} k_n m_{ij}^{\vert}}$
Tangential damping	$\gamma_{t,ij} = 2 \sqrt{\frac{5}{6}} \nabla \frac{\ln(e_r)}{\sqrt{\ln^2(e_r) + \pi^2}} \sqrt{k_t m_{ij}^{\vert}}$
Coulomb friction force	$\boldsymbol{f}_{ct,ij} \vert \quad \mu_{s,ij} \boldsymbol{f}_{cn,ij} \frac{\boldsymbol{\delta}_{t,ij}}{\sqrt{\boldsymbol{\delta}_{t,ij}} \nabla}$
Torque by tangential force	$\boldsymbol{M}_{t,ij} = \boldsymbol{r}_i \otimes (\boldsymbol{f}_{ct,ij})$
Rolling friction torque	$\boldsymbol{M}_{r,ij} = \mu_{r,ij} \boldsymbol{f}_{cn,ij} \frac{\boldsymbol{\omega}_{p,ij}}{\sqrt{\boldsymbol{\omega}_{p,ij}} \nabla} R_{ij}^{\vert}$
Equivalent mass	$\frac{1}{m_{ij}^*} = \frac{1}{m_i} + \frac{1}{m_j}$
Equivalent radius	$\frac{1}{R_{ij}^*} = \frac{1}{R_i} + \frac{1}{R_j}$
Equivalent Young's modulus	$\frac{1}{Y_{ij}^*} = \frac{\left(1 \quad \nu_i^2\right)}{Y_i} + \frac{\left(1 \quad \nu_j^2\right)}{Y_j}$
Equivalent shear modulus	$\frac{1}{G_{ij}^*} = \frac{2(2+\nu_i)(1 \quad \nu_i)}{Y_i} + \frac{2(2+\nu_j)(1 \quad \nu_j)}{Y_j}$
Sliding friction coefficient	$\mu_{s,ij}$
Rolling friction coefficient	$\mu_{r,ij}$
Distance to contact point for particle i	$\boldsymbol{r}_i$
Radius of particle i	R_i

Table 2: Equations for the DEM model adapted from [19]

2.2. Equations of motion for the liquid phase (CFD)

Due to the presence of particles in the system, the classical NS equations had to be adapted. To do this, the volume average Navier-Stokes equations (VANS), which take the void fraction (ϵ_f) into account, are commonly used. There are different formulations that mainly depend on the multiplication of the pressure gradient by ϵ_f. For the present study, we began with Form A of these equations [26]. For more details, we refer to [34, 77]. Form A in a rotating frame of reference is given by:

$$\frac{\partial}{\partial t}(\epsilon_f \rho_f) + \quad \times(\epsilon_f \rho_f \boldsymbol{u}) = 0 \tag{5}$$

$$\frac{\partial}{\partial t}(\epsilon_f \rho_f \boldsymbol{u}_f) + \quad \times(\epsilon_f \rho_f \boldsymbol{u}_f \leq \boldsymbol{u}_f) = \quad \epsilon_f \quad p + \quad \times\boldsymbol{\tau} + \epsilon_f \boldsymbol{F}_g$$

$$\underbrace{\frac{1}{\Delta V} \sqrt{\sum_i^{n_p} (\boldsymbol{f}_{pf,i} \quad \boldsymbol{f}_{\ p,i} \quad \boldsymbol{f}_{\ *\boldsymbol{\tau},i})}}_{\boldsymbol{F}_{pf}} \quad \epsilon_f \quad 2\rho_f \boldsymbol{\Omega} \otimes \boldsymbol{u}_f + \rho_f \boldsymbol{\Omega} \otimes (\boldsymbol{\Omega} \otimes \boldsymbol{q}_f) \Big(\tag{6}$$

$$\text{with} \quad \boldsymbol{f}_{pf,i} = \boldsymbol{f}_{drag,i} + \boldsymbol{f}_{Ar,i} + \boldsymbol{f}_{\ *\boldsymbol{\tau},i} + \boldsymbol{f}_{\ p,i} + \sqrt{\ } \boldsymbol{f}_{add,i} \tag{7}$$

where $\boldsymbol{F}_g$ represents gravity, $\boldsymbol{F}_{pf}$ represents the global momentum exchange between the fluid and the particles, and $\boldsymbol{f}_{pf,i}$ represents the interaction force between the fluid and a particle i. This force includes the drag force $\boldsymbol{f}_{drag,i}$, the Archimedes force $\boldsymbol{f}_{Ar,i}$, the viscous forces $\boldsymbol{f}_{\ *\boldsymbol{\tau},i}$, the pressure gradient forces

$\boldsymbol{f}_{p,i}$ and $\boldsymbol{f}_{add,i}$ which represents the different interaction forces between a particle and a fluid in an unsteady regime such as the virtual mass force, the Basset force, and the lift forces (Magnus and Saffman) [26]. Lastly, the viscous stress tensor is defined as:

$$\boldsymbol{\tau} = \epsilon_f \mu \Big)(\quad \boldsymbol{u}) + (\quad \boldsymbol{u})^T \quad \frac{2}{3}(\quad \times \boldsymbol{u}) \mathbb{I} \sum \tag{8}$$

where μ is the dynamic viscosity and $\mathbb{I}$ is the identity tensor.

2.3. CFD-DEM coupling applied to solid-liquid mixing operations

CFD-DEM simulations require a large number of parameters. The objective of the present section is to describe those that have a substantial impact on its application to solid-liquid mixing simulations.

2.3.1. Viscosity model

It is important to take into account the presence of particles in the calculation of the viscosity. Einstein and Batchelor have shown that variations in viscosity in the presence of particles is due to the disturbances they generate within the fluid flow [13] at the particle scale. However, it is important to recall that, with the unresolved CFD-DEM approach used in the present work, the flow is solved at a larger scale than the particle scale. It thus is impossible to capture

variations in viscosity with such a model. This was proven and discussed by Blais et *al.* [19], who showed that the addition of a viscosity model that takes the void fraction into account is necessary. In the present study, the Krieger-Dougherty model [43] was used:

$$\mu = \mu_0 \Big)1 \quad \frac{\epsilon_p}{\epsilon_p^{|}} \sum^{[\eta]\epsilon_p^*} \tag{9}$$

where $[\eta]$ is the intrinsic viscosity evaluated at 2.5 in this model for spheres, $\epsilon_p^{|}$ is the maximum packing fraction, which is taken to be 0.64 for single-size spherical particles [12], and μ_0 is the initial viscosity of the fluid.

225 *2.3.2. Smoothing of the momentum exchange force*

In the present study, the divided approach was used to project the particle on the fluid grid to calculate the void fraction [19]. In this approach, the particle is divided into 27 equal volumes, and the position of each centroid is projected on the fluid grid to calculate the void fraction. This strategy allows a first smoothing of the coupling term between fluid and particle but it may be insufficient to obtain good stabilization of the coupling scheme. Different additional strategies have been described in the literature [60] but, based on the conclusive results of the CFD-DEM model reported by [17, 18], we used the isotropic diffusive smoothing approach. For a quantity ζ, a parabolic filter is

applied based on the equation:

$$\frac{\partial \zeta}{\partial t} = \frac{\lambda^2}{\Delta t_{CFD}} \quad ^2(\zeta) \tag{10}$$

where λ is the characteristic smoothing length chosen equal to $3d_p$ to ensure stability. This smoothing process is illustrated in Figure 3 for a fluid cell (numbered 1) containing 3 particles (α, β, γ). The interaction forces for each particle are noted $\boldsymbol{f}_{pf,\alpha,\beta,\gamma}$ (Figure 3 (a)). The total resultant force for cell 1 is equal to the sum of all these forces and is applied to the center of the cell (Figure 3 (b)). For simplicity this illustration is made in 2 dimensions but in reality in our model in 3 dimension this smoothing is made on 27 cells and not 9.

$$\boldsymbol{F}^1_{pf} = \boldsymbol{f}_{pf,\alpha} + \boldsymbol{f}_{pf,\beta} + \boldsymbol{f}_{pf,\gamma} \tag{11}$$

In the case where a smoothing is added, the force concentrated in the center of the cell is conservatively distributed to the neighboring cells (Figure 3 (c)) such that:

$$\boldsymbol{F}^1_{pf} = \sum_{i=1}^{9} \boldsymbol{f}^i_{pf} \tag{12}$$

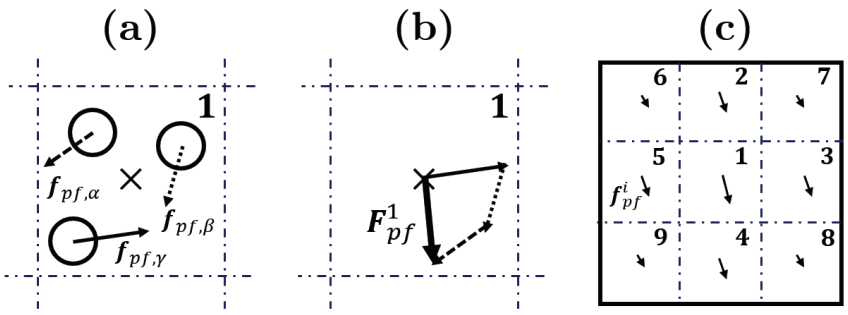

Figure 3: Illustration of isotropic diffusive smoothing (a) start of the CFD time step (b) result obtained without smoothing (c) result obtained by applying the smoothing method. The higher the parameter λ is, the more the force considered in cell 1 will be distributed to the neighboring cells.

2.3.3. Coupling Strategy

In the CFDEM platform an implicit strategy for the momentum exchange between liquid and solid is generally used. The coupling force F_{pf} of the momentum VANS equation (6) is replaced by a semi-implicit strategy:

$$\boldsymbol{F}_{pf} = K_{pf}(\boldsymbol{u}_p - \boldsymbol{u}_f) \tag{13}$$

$$\text{with} \quad K_{pf} = \frac{|\boldsymbol{F}_{pf}|}{|\boldsymbol{u}_p - \boldsymbol{u}_f|} \tag{14}$$

A direct consequence of this coupling strategy is the generation of an interaction force if the average velocity of the particles is not perfectly equal to the velocity of the fluid in a particular cell. This is particularly problematic in a rotating frame of reference and more generally for rotating systems. Indeed, in this kind

of frame, additional conditions must be imposed on the angular velocity of the particle and the fluid. Even if the applied angular velocities are equal, the topology of the mesh used could have a dramatic impact on the entire stability of the system (Figure 4). Indeed, in our case, the further the cells are from the center of the system, the more deformed they become and the more uneven the distribution of particles in the same cell is. The topology of the mesh leads to more particles near the external edge of a cell. However, the linear velocity of the particles is proportional to the distance from the center (ωr with r the distance from the center). Thus, the closer the particle is to the external edge of a cell, the greater its linear velocity. This is all the more problematic as the cell is far from the center of rotation because the velocity of the particles is higher and the cells are generally more deformed. This has two consequences that are illustrated in Figure 4:

- In a fluid cell, since the particles are non-uniformly distributed, the barycentre of the particles is displaced to the zone of high particle concentration.
- Most particles are located near the external edge of a fluid cell because of the topology of the mesh. However, the linear velocity is higher near the external edge because it is further from the center. Thus, the average

particle velocity u_p in a cell is higher than if the particles are uniformly distributed. This is not the case for the fluid where the velocity is directly applied to the center of the cell. Consequently, the further the cells are from the center, the higher the difference between the solid velocity and the flow velocity in the fluid cell considered.

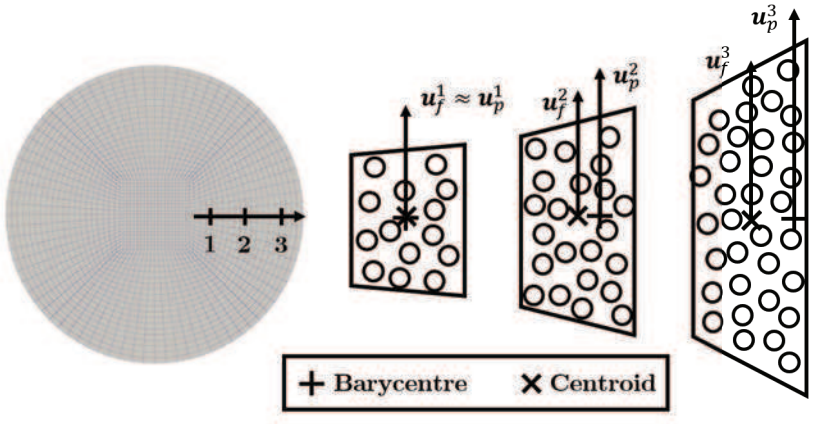

Figure 4: Illustration of the impact of the mesh topology on the difference in velocity $\boldsymbol{u}_p - \boldsymbol{u}_f$ for the three fluid cells 1,2,3. Here $\boldsymbol{u}_p^1 < \boldsymbol{u}_p^2 < \boldsymbol{u}_p^3$ and $\boldsymbol{u}_f^1 < \boldsymbol{u}_f^2 < \boldsymbol{u}_f^3$ but $\boldsymbol{u}_p^1 - \boldsymbol{u}_f^1 < \boldsymbol{u}_p^2 - \boldsymbol{u}_f^2 < \boldsymbol{u}_p^3 - \boldsymbol{u}_f^3$.

This problem is illustrated using a structured hexahedral mesh. However, unstructured meshes face the same problem. To avoid this problem it is preferable to use explicit coupling. This implies that the formulation $K_{pf}(\boldsymbol{u}_p - \boldsymbol{u}_f)$, which is characteristic of an implicit coupling, is no longer used. In the case of

an explicit coupling, the particle-fluid force $\boldsymbol{F}_{pf}$ is applied directly without any averaging. This change in the coupling strategy alters the maximal coupling time step that can be used. This has been extensively analyzed by Blais et *al.* in [19].

2.3.4. Force model

In a CFD-DEM model, the choice of the interaction forces between the two phases can play a major role in the accuracy of the simulations. In the specific case of solid-liquid mixing, this problem has been widely studied. Ljungqvist et *al.* [46] concluded that the drag force is the main source of momentum exchange. Moreover, in the case of a significant density ratio between the solid and the fluid ($\frac{\rho_p}{\rho_f} > 1$), the effects of the virtual mass force are negligible compared with the drag force. This was verified by Tatterson et *al.* [73] and confirmed by more recent results from solid suspension studies [37, 71]. It has also been shown that, for this kind of application, the Basset force has a negligible impact compared with the drag force [18, 41]. Lastly, based on previous studies [17, 33], we decided to disregard the impact of lift forces (Magnus and Saffman). The forces retained and used in the present model are detailed in Table 3. Two different drag models were tested (Di Felice model [30] and Rong model [63]).

Force	Equation
Pressure gradient	$\frac{\pi}{6}d_p^3 \quad p$
Viscous force	$\frac{\pi}{6}d_p^3 \quad \times\tau$
Archimedes' force	$-\rho_f V_p \boldsymbol{g}$
Drag force - Di Felice model	$\frac{1}{8}C_D\rho_f\pi d_p^2\epsilon_f^2 \quad ^{X_i} \quad \boldsymbol{u}_f \quad \boldsymbol{u}_p \quad (\boldsymbol{u}_f \quad \boldsymbol{u}_p)$
- Rong model	$\frac{1}{8}C_D\rho_f\pi d_p^2\epsilon_f^2 \quad ^{\beta(\epsilon_f)} \quad \boldsymbol{u}_f \quad \boldsymbol{u}_p \quad (\boldsymbol{u}_f \quad \boldsymbol{u}_p)$
	$\beta(\epsilon_f) = 2.65(\epsilon_f + 1) \quad (5.3 \quad 3.5\epsilon_f)\epsilon_f^2 \exp\Big) \frac{(1.5 \quad \log(R_{ep}))^2}{2}\Big($
	$X_i = 3.7 \quad 0.65 \exp\Big) \frac{(1.5 \quad \log(R_{ep}))^2}{2}\Big($
	$C_D = \Big)0.63 + \frac{4.8}{\sqrt{R_{ep}}}\Big)^2$
	$R_{ep} = \frac{d_p\epsilon_f\|\boldsymbol{u}_f \quad \boldsymbol{u}_p\|\rho_f}{\mu_f}$

Table 3: Expression of the forces used in the CFD-DEM model.

2.3.5. Non-inertial frame: boundary and initial conditions

To conclude the description of the model, it is important to present the various initial steps that are necessary for CFD-DEM simulations in a non-inertial frame. A simulation in a rotating frame of reference implies setting specific initial and boundary conditions on the fluid, the particles, and the geometrical components. Indeed, as the whole problem is reformulated in the reference frame of the agitator, the impeller remains motionless during the simulations but the particles, the fluid, and the tank must be in motion from $t = 0$. The different initial steps for the simulation of a mixing system are described and summarized in Figures 5.

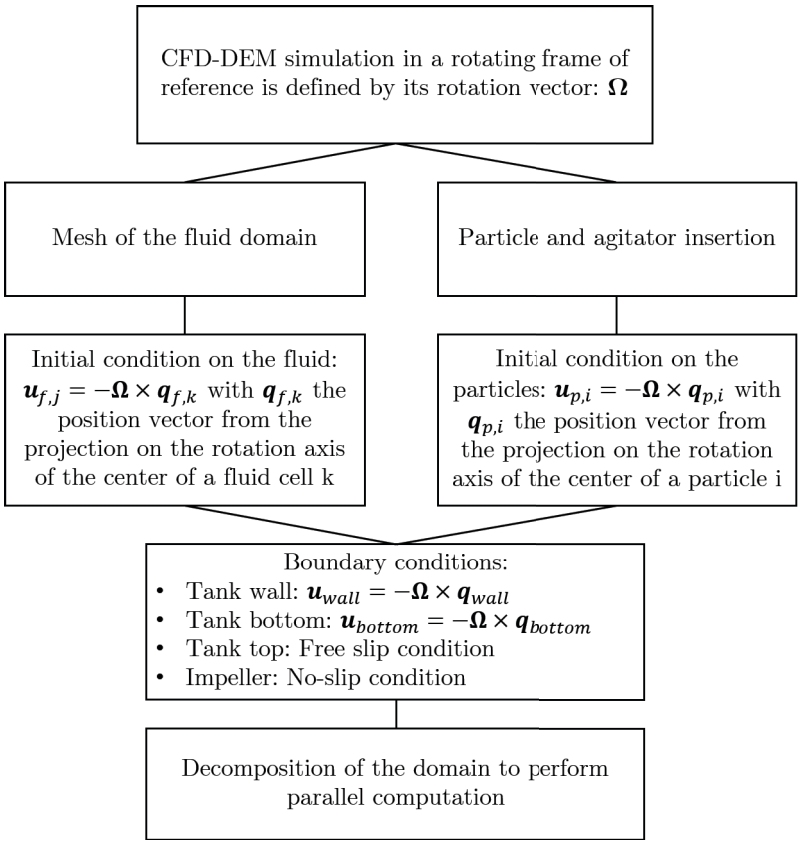

Figure 5: Initial and boundary conditions of a CFD-DEM experiment in a rotating frame of reference.

3. Taylor Couette CFD-DEM simulation

Single rotating reference frame methods (SRF) have been implemented in the past and have been used for independent CFD and DEM simulations [28, 65] and for CFD-DEM simulations where the fluid is a gas [64]. In the present study, we evaluate the possibility of performing CFD-DEM in a rotating frame of reference where the fluid is a liquid with a density of 1390 kg/cm^3 and a constant viscosity of 1 Pa.s. We start with the simple setup of a single 3 mm diameter particle with a density of 2500 kg/cm^3 inserted in a Taylor-Couette flow. The aim of this first test case is to compare the trajectory of the particle as it is simulated in the two frames.

In the Eulerian frame of reference, the inner wall is in rotation at a constant angular velocity Ω= 20 rad/s whereas the outer wall is fixed with a no-slip boundary condition. In the Lagrangian rotating frame, the inner wall is fixed and the outer wall is in rotation at an angular velocity opposite to that of the frame (-20 rad/s). A single particle is then inserted into the fluid, and the right initial angular velocity is applied on the particle and the fluid in the rotating frame of reference (Figure 5).

Figure 6 shows the trajectories of the particle after the same time of sim-

ulation of 1s in the two different frames. Then to compare these results we rotate the coordinates and we observe very good agreement between the two simulations.

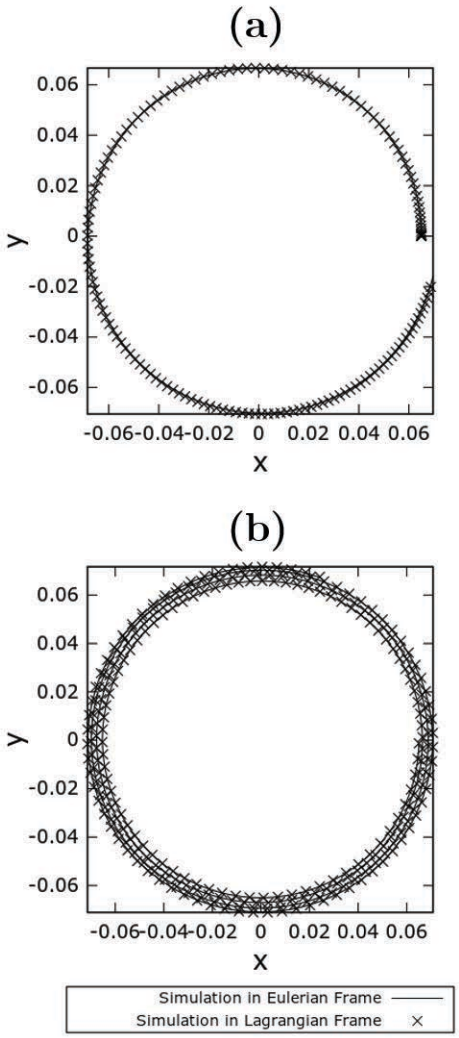

Figure 6: Visualisation of the trajectory of the particle in the two different frames of reference for a velocity of 20rad/s : (a) in the Eulerian frame and (b) in the Lagrangian frame.

4. CFD-DEM in a non-inertial frame with N particles

After studying the behavior of a single particle, we focus on the stability of CFD-DEM simulations in a rotating frame of reference with more particles. We consider a tank of fluid loaded with $150,000$ particles. In the Eulerian frame of reference, the particles are static during the entire simulation. The test is aimed at determining whether, after the change of frame of reference, the particle bed remains stable at the bottom and rotates without any axial movement in the Lagrangian frame of reference. All the CFD, DEM, coupling, and geometric parameters used in this experiment are given in Table 4.

We performed the experiment with different CFD-DEM solvers:

- Solver #1: cfdem-PISO-SRF-implicit-VANS: CFD-DEM solver based on the PISO algorithm [39], with an implicit coupling for the momentum between the fluid and the particles. The equations for the fluid are Form A of the VANS equations.

- Solver #2: cfdem-PISO-SRF-explicit-VANS: CFD-DEM solver based on the PISO algorithm with an explicit coupling for the momentum between

Parameter	Symbol	Value
Young's Modulus	Y	100 MPa
Cofficient of restitution	e_r	0.9
Poisson's ratio	ν	0.25
Coefficient of friction	μ_s	0.3
Rolling friction	μ_r	0.1
DEM time step	Δt_{DEM}	$5 \otimes 10^{-6}$ s
CFD time step	Δt_{CFD}	$5 \otimes 10^{-5}$ s
Coupling time step	Δt_c	$5 \otimes 10^{-5}$ s
Particle diameter	d_p	3 mm
Particle density	ρ_p	2500 kg/cm^3
Volume fraction	X_v	5.7% (148700 particles)
Fluid density	ρ_f	1390 kg/cm^3
Initial dynamic viscosity	μ_0	1 Pa.s
Tank diameter	T	0.365 m
Tank height	H	0.365 m
Angular velocity	Ω	250 RPM
Mesh	$n_x \otimes n_y \otimes n_z$	$20 \otimes 20 \otimes 80$

Table 4: CFD-DEM simulation parameter for the case of the loaded tank without impeller.

The time steps were calculated based on the results of [19].

the fluid and the particles. The equations for the fluid are Form A of the VANS equations.

- Solver #3: cfdem-PISO-SRF-explicit-NS: CFD-DEM solver based on the PISO algorithm with an explicit coupling for the momentum between the fluid and the particles. The equations for the fluid are the classical NS equations.

First, with solver #1 and its implicit coupling we observe a destabilization of the bed of particles close to the wall. This result was expected for the reason discussed in the Section 2.3.3 where we showed that implicit coupling leads to a fictitious coupling force between the fluid and particles for rotating systems.

However, an unexpected detachment of the particles near the center of the tank is obtained with the solver #2. This is the consequence of oscillations in the void fraction field (ϵ_f) caused by the projection of the particle volume on the mesh. Indeed, if we refer to the continuity equation of the VANS equations (Eq.5), it implies that the velocity field is not divergence-free as $\nabla \times \boldsymbol{u}_f = \frac{1}{\epsilon_f}\left(\frac{\partial \epsilon_f}{\partial t}\boldsymbol{u}_f \times \epsilon_f\right)$ and not $\nabla \times \boldsymbol{u}_f = 0$. This has a direct impact on the expression of the viscous stress tensor. Instead of having null stress at $t = 0$, stresses that we qualify as fictitious are established in the particle bed close to

oscillations in the void fraction. To avoid this instability, we decided to not consider the void fraction in the resolution of the fluid motion by developing solver #3 based on the classical form of the NS equations. Using this solver, we obtain the desired result with a stable particle bed. This experiment shed light on the fact that with systems in motion at $t = 0$, as is the case for studies using rotating frames of reference, the VANS equations appear to be unstable.

5. Comparison with experimental results

After obtaining conclusive results on the feasibility of conducting CFD-DEM experiments in a rotating frame of reference, we validate the model for the case of solid-liquid mixing. Our validation process is based on numerical and experimental results previously obtained by Blais et *al.* [16, 18, 19] and Lassaigne et *al.* [45] for an agitated tank with a pitched blade turbine. The numerical results in [18, 19] were obtained with a CFD-DEM model in an Eulerian frame of reference with an immersed boundary approach.

This section is divided into three parts. The first is devoted to the description of the system used, the second to the qualitative validation based on flow patterns and solid distribution, and the third to the quantitative results for the fraction of suspended particles.

5.1. Description of the system

The physical parameters used are the same as those in the previous section (see Table 4). The geometry used is described in Table 5 and Figure 7. This set up corresponds exactly to the one used in [18, 19, 45].

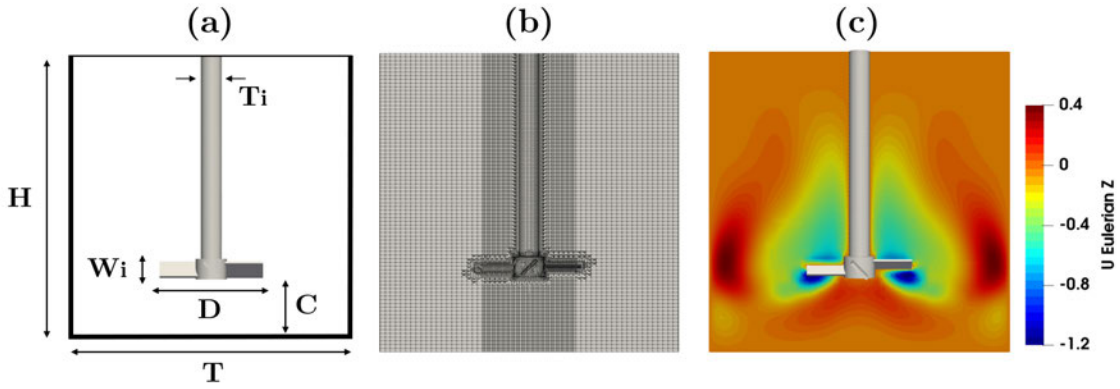

Figure 7: Simulation of solid-liquid mixing with a PBT: (a) geometrical parameters (b) sectional view of the mesh used (c) sectional view of the axial fluid velocity with a CFD-DEM simulation in the Lagrangian frame for $N = N_{js} = 425RPM$.

5.2. Visual validation

Mixing with a down pumping PBT lead to well-known flow patterns. One of the main characteristics of this impeller is that it generates a mixed flow combining axial and radial components (Figure 7 (c)).

For solid-liquid mixing, this leads to the formation of a cone of particles

Element	Symbol	Dimension
Tank diameter	T	36.5 cm
PBT diameter	D	$\frac{T}{3}$
Liquid height	H	T
Off-bottom clearance	C	$\frac{T}{4}$
PBT blade height	W_i	$\frac{D}{5}$
Shaft diameter	T_i	$\frac{D}{5}$

Table 5: Geometrical parameters used for the simulation of a mixing system with a PBT

just bellow the shaft. This phenomenon is well documented and has already been reported numerically and experimentally [19, 45]. It is important to note that our model is able to reproduce this hydrodynamic phenomenon (Figure 8). We then compare the shape of this cone to the shapes of the cones obtained experimentally [45] or numerically with the CFD-DEM model based on the immersed boundary method [18, 19]. For this purpose, we compare the ratio between the diameter of the cone base and the diameter of the tank. This is shown in Figure 8. We note that the experimental set up contains 48 electrodes which were used for tomography measurements.

The comparison between the shape of the different cones provides important information on the capacity of our numerical model to reproduce the hydrodynamic phenomena that occur in a mixing tank. The different measurements

at different agitation speeds are presented in Table 6. These results show very good agreement between the different measurements.

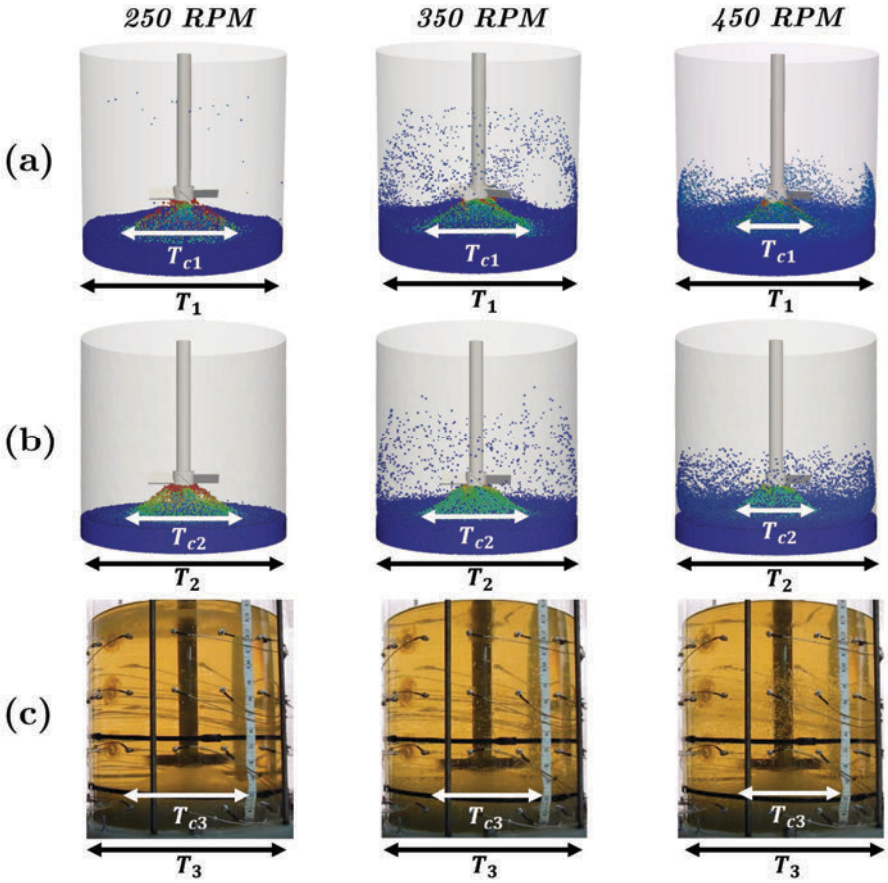

Figure 8: Illustration of the formation of the cone of particles at different agitation speeds: (a) with a CFD-DEM model using the immersed boundary method, (b) with our CFD-DEM model in a rotating frame of reference, and (c) experimentally.

A second characteristic phenomenon of down-pumping agitation with a PBT is the formation of a low concentration zone of particles near the shaft. The form

Method	250 RPM	350 RPM	450 RPM
Immersed boundary	$\frac{T_{c1}}{T_1} = 0.54$	$\frac{T_{c1}}{T_1} = 0.48$	$\frac{T_{c1}}{T_1} = 0.37$
Rotating frame	$\frac{T_{c2}}{T_2} = 0.54$	$\frac{T_{c2}}{T_2} = 0.50$	$\frac{T_{c2}}{T_2} = 0.36$
Experimentally	$\frac{T_{c3}}{T_3} = 0.57$	$\frac{T_{c3}}{T_3} = 0.50$	$\frac{T_{c3}}{T_3} = 0.42$

Table 6: Comparison of the dimensions of cones obtained experimentally and with differents numerical methods for three different Reynolds numbers $Re = 86 - 121 - 155$.

of this zone is particularly noteworthy because it is toroidal. This phenomenon is well known for single-phase systems [24] and has also been observed with multiphase systems [19]. The results obtained with our CFD-DEM model in a rotating frame of reference for the distribution of the particles in the tank are shown in Figure 9 and illustrate the presence of this characteristic zone very well.

5.3. Quantitative results

To further confirm that our new model can predict the dynamics of solid-liquid mixing, it is necessary to validate its capacity to predict the fraction of suspended particles, in other words the number of particles suspended relative to the total number of particles. In the simulations, this fraction is measured by Lagrangian suspension fraction analysis (LSFA). This method considers a par-

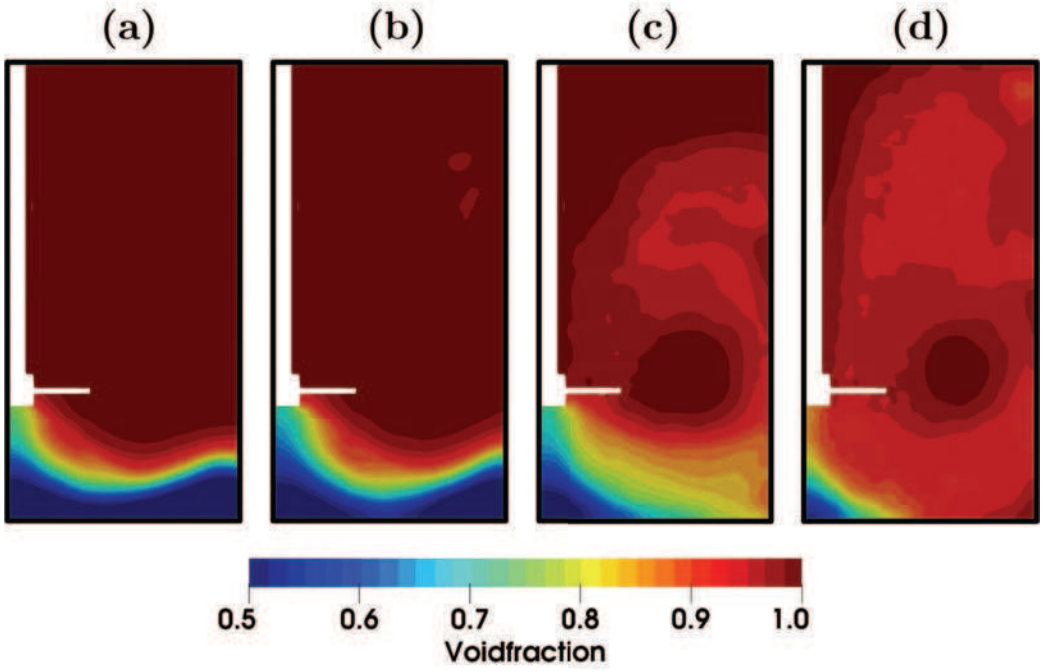

Figure 9: Sectional view in the $y - z$ plane of the void fraction after 50 s of agitation at different rotational speeds: (a) 250RPM, (b) 350RPM, (c) 450RPM, and (d) 700RPM.

ticle as suspended if it has moved a certain distance Δz_{js} in the axial direction during a certain time Δt_{js}. For more details about this method we refer to [19]. The results obtained are presented in Figure 10.

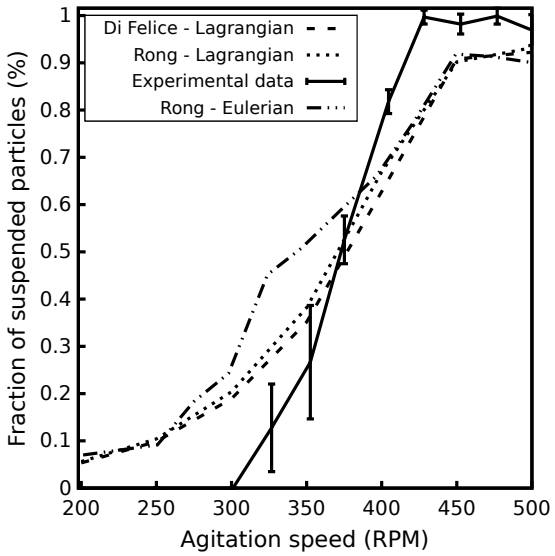

Figure 10: Comparison of the suspension curves obtained experimentally [45] and numerically with the CFD-DEM model in the Eulerian frame based on the immersed boundary method [19] and with our CFD-DEM model in the Lagrangian frame of reference. The pressure gauge technique was used experimentally to measure the suspended fraction. The LSFA method was used numerically to measure the suspended fraction, with the following criteria: $\Delta z_{js} = d_p$ and $\Delta t_{js} = 2$ s.

It is important to note that we are able to predict the experimental value of N_{js}, which is approximatively 425RPM. To compare, for the same system

the Zwietering correlation gives a value of Njs of 800RPM [45]. However, we observe a difference in the fraction of suspended particles at high and low agitation speeds. We recall that the experimental measurements were made using the pressure gauge technique [49]. In Figure 10 we can see that the pressure gauge technique indicated that 100% of the particles are suspended at 450RPM. However, some particles are still retained in the cone below the agitator at this speed. Similarly, in Figure 10 we can see that no particles are suspended at 250RPM whereas the cone is in formation at this speed. We conclude that the pressure gauge technique does not take the cone of particles into account in variations of the fraction of suspended particles. This can be explained by the damping of the fluid, which is a phenomenon that is all the more important when the viscosity of the fluid is high. This is the main reason for the differences between the numerical and experimental results.

Moreover, if we compare the numerical results obtained with the SRF (Lagrangian) and the immersed boundary (Eulerian) approaches, we can see that the model in a rotating frame of reference does not exhibit a "jump" in the fraction of suspended particles at an agitation speed close to 325RPM. This "jump" is also absent from the experimental data. We believe that this "jump" is a numerical artefact, as the immersed boundary method uses a fictitious forcing

term directly inserted in the NS equations, which may lead to an over forcing of the fluid when the impeller starts to move. Additionally, from Figure 10 we can see that the Di Felice and Rong formulations for the drag model give quasi-identical results.

All simulations were carried out on the Cedar cluster of Compute Canada. Each simulation used 16 cores of an Intel Xeon E5-2683 v4 processor. The distribution of the cores is based on a splitting of the domain into 4 levels with 4 sub-domain per level. Each simulation was carried out for 12 days of wall time for one physical minute of mixing.

6. Double helical ribbon

We recall that the main advantage of our model and what differentiates it from other approaches is that it is suitable for all impeller configurations that present axial symmetry. We thus conclude the present study with an examination of a complex close-clearance agitator often used in viscous mixing: the double helical ribbon (DHR).

6.1. Description of the system

For this experiment, we keep the same physical properties for the fluid and the particles (see Table 4). All the geometrical parameters used for this exper-

iment are described in the Table 7 and Figure 11.

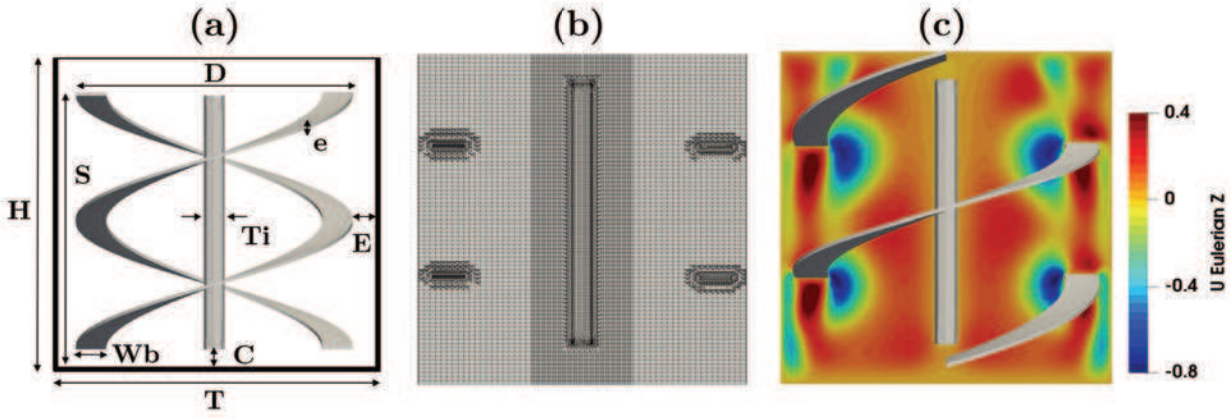

Figure 11: Simulation of solid-liquid mixing with a DHR: (a) geometrical parameters (b) sectional view of the mesh used (c) sectional view of the axial fluid velocity with a CFD-DEM simulation in the Lagrangian frame for $N = N_{js} = 200RPM$.

6.2. Results

We begin by observing the flow pattern that occurs with DHR in the context of solid-liquid mixing (Figure 11 (c)). The bulk of the velocity in the DHR flow is in the axial direction ($\boldsymbol{e}_z$). It consists of two upward flows, one along the wall of the vessel near the ribbons and one close to the center along the shaft axis.

In addition, in Figure 12 we see the evolution of the void fraction with the agitation speed. The particles preferentially suspend near to the center along the shaft. This is perfectly consistent with the observations for the components

Element	Symbols	Dimension
Tank diameter	T	36.5 cm
Ribbon diameter	D	33.3 cm
Liquid height	H	T
Ribbon height	S	28.7 cm
Close clearance	C	$\frac{T}{8}$
Distance to the wall	E	1.6 cm
Ribbon thickness	e	0.4 cm
Ribbon width	W_b	3.6 cm
Shaft diameter	T_i	2.54 cm
Pitch	s	S

Table 7: Geometrical parameters used for the simulation of the mixing system and its double helical ribbon.

of the fluid velocity.

Lastly, we conclude with some quantitative results and the determination of N_{js}, which is shown in Figure 12 and estimated to be $200RPM$. To go further and compare the efficiency of the double ribbon against the PBT, it would be necessary to anlayse the mixing dynamics at equivalent power consumption.

7. Conclusion

Sixty years after Zwietering, the design of solid-liquid mixing operations remains a challenge because of the different physical phenomena that occur at different scales in such systems. There is a lack of studies on the laminar regime of operation. This paper focuses on the study of viscous solid-liquid mixing, which is a major issue for many industries. The main objective of the present study was to develop a numerical model able to simulate solid-liquid mixing operations in the laminar regime.

We realized that one of the main issues with this type of regime was the modeling of traditionally used complex impellers. To cope with this issue, we decided that the rotating frame approach was the most appropriate. Moreover, to obtain an optimally accurate description of particle and fluid motion with a reasonable computing time, we decided to use an unresolved CFD-DEM method.

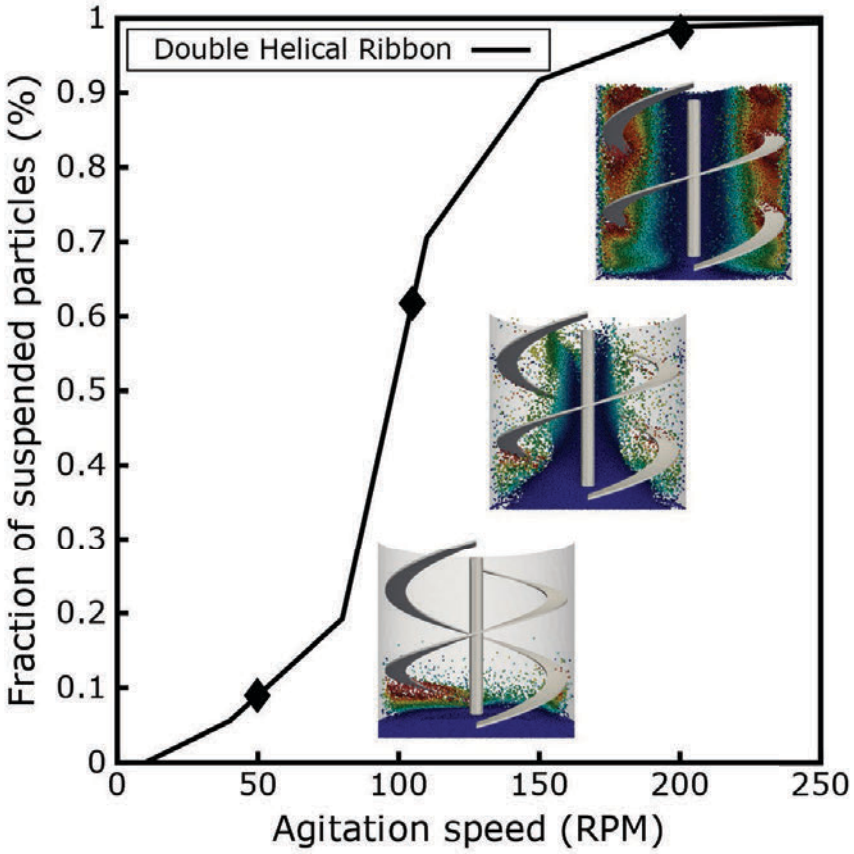

Figure 12: Suspension curve obtained numerically with our CFD-DEM model in the Lagrangian frame for a mixing system with a double helical ribbon.

In addition to providing additional knowledge with respect to viscous solid-liquid mixing, the possibility of performing CFD-DEM in a non-Galilean frame was thus studied, which had never been done before.

This work was carried out using the CFDEM framework. The model was developed incrementally with test cases of increasing complexity and ended with the experimental comparison against an agitated system with a pitched blade turbine. Lastly, we concluded that, in order to obtain a numerical model that faithfully describes the physical phenomena occurring in a mixing tank, it is necessary to use an explicit coupling and an additional smoothing parameter for the momentum exchange between the solid and liquid phases. We also showed that the VANS equations must be used with care with rotating systems as, in our case, they led to severe instabilities. This seemed to be a consequence of the particular expression of the viscous stress tensor due to the fact that the velocity fields were not divergence-free with the VANS equations. The resulting model was finally used to study solid-liquid mixing with a close clearance impeller: the double helical ribbon. It is important to note that this model is only suitable for rotationally invariant geometry. Thus, systems with baffles or even with eccentric agitators cannot be studied with this approach.

In summary, the main contribution of this work is to provide a CFD-DEM

model in a rotating frame of reference that is able to reproduce the different phenomena occurring in a solid-liquid mixing system with very good reliability. The present study proved that it is possible to perform CFD-DEM simulations in a non-inertial frame of reference, which opens up a wide range of applications. For example, we could consider using this type of model to study rotary drying systems or rotating drums.

8. Acknowledgements

The financial support from the Natural Sciences and Engineering Research Council of Canada (NSERC) is gratefully acknowledged. Computations were made on supercomputers Cedar and Graham managed by Compute Canada. In particular, the authors would like to acknowledge the efficient support received from Calcul Québec and Compute Canada systems analysts.

References

[1] LIGGGHTS. (2011). LAMMPS improved for general granular and granular heat transfer simulations. Retrieved from http://www.liggghts.com.

[2] CFDEM, CFDEM-Opensource CFD, DEM and CFD–DEM. https://www.cfdem.com/, 2020.

[3] OpenCFD, OpenFOAM – the opensource CFD toolbox. https://www.openfoam.com/, 2020.

[4] Alessandro Tamburini, Andrea Cipollina, and Giorgio Micale. Cfd simulation of solid liquid suspensions in baffled stirred vessels below complete suspension speed. *Chemical Engineering Transactions*, 24:1435–1440, April 2011.

[5] R. Angst and M. Kraume. Experimental investigations of stirred solid/liquid systems in three different scales: Particle distribution and power consumption. *Chemical Engineering Science*, 61(9):2864–2870, 2006.

[6] P.M. Armenante, E.U. Nagamine, and J. Susanto. Determination of correlations to predict the minimum agitation speed for complete solid suspension in agitated vessels. *Canadian Journal of Chemical Engineering*, 76(3):413–419, 1998.

[7] VICTOR A. Atiemo-Obeng, W. R. Penney, and Piero Armenante. Solid-liquid mixing. *Handbook of industrial mixing: Science and practice*, pages 543–584, 2004.

[8] Inci Ayranci and Suzanne M. Kresta. Critical analysis of Zwietering corre-

lation for solids suspension in stirred tanks. *Chemical Engineering Research and Design*, 92(3):413–422, March 2014.

[9] Inci Ayranci, Theodore Ng, Arthur W. Etchells, and Suzanne M. Kresta. Prediction of just suspended speed for mixed slurries at high solids loadings. *Chemical Engineering Research and Design*, 91(2):227–233, 2013.

[10] A. Bakker and L. E. Gates. Properly choose mechanical agitators for viscous liquids. *Chem. Eng. Prog.*, 91(12):25–34, December 1995.

[11] G_ Baldi, R. Conti, and E. Alaria. Complete suspension of particles in mechanically agitated vessels. *Chemical Engineering Science*, 33(1):21–25, 1978.

[12] H. A. Barnes, J. F. Hutton, and K. Walters. *An Introduction to Rheology*. Elsevier, June 1989.

[13] G. K. Batchelor and J. T. Green. The determination of the bulk stress in a suspension of spherical particles to order c 2. *Journal of Fluid Mechanics*, 56(3):401–427, 1972.

[14] Ariane Bérard, Gregory S. Patience, and Bruno Blais. Experimental Meth-

ods in Chemical Engineering: Unresolved CFD-DEM. *The Canadian Journal of Chemical Engineering*, 2020.

[15] Olivier Bertrand, Bruno Blais, François Bertrand, and Louis Fradette. Complementary methods for the determination of the just-suspended speed and suspension state in a viscous solid–liquid mixing system. *Chemical Engineering Research and Design*, 136:32–40, August 2018.

[16] Bruno Blais. *Développement d'un modèle Euler-Lagrange robuste pour la simulation des écoulements solide-liquide dans les opérations de mélange*. PhD thesis, Polytechnique Montréal, 2016.

[17] Bruno Blais and François Bertrand. CFD-DEM investigation of viscous solid–liquid mixing: Impact of particle properties and mixer characteristics. *Chemical Engineering Research and Design*, 118:270–285, February 2017.

[18] Bruno Blais, Olivier Bertrand, Louis Fradette, and François Bertrand. CFD-DEM simulations of early turbulent solid–liquid mixing: Prediction of suspension curve and just-suspended speed. *Chemical Engineering Research and Design*, 123:388–406, 2017.

[19] Bruno Blais, Manon Lassaigne, Christoph Goniva, Louis Fradette, and François Bertrand. Development of an unresolved CFD–DEM model for

the flow of viscous suspensions and its application to solid–liquid mixing. *Journal of Computational Physics*, 318:201–221, August 2016.

[20] Bruno Blais, Manon Lassaigne, Christoph Goniva, Louis Fradette, and François Bertrand. A semi-implicit immersed boundary method and its application to viscous mixing. *Computers & Chemical Engineering*, 85:136–146, February 2016.

[21] Bruno Blais, David Vidal, Francois Bertrand, Gregory S. Patience, and Jamal Chaouki. Experimental Methods in Chemical Engineering: Discrete Element Method—DEM. *The Canadian Journal of Chemical Engineering*, 97(7):1964–1973, 2019.

[22] David AR Brown, P. N. Jones, John C. Middleton, George Papadopoulos, and Engin B. Arik. Experimental methods. *Handbook of industrial mixing: science and practice*, pages 145–256, 2004.

[23] Alberto Brucato, Michele Ciofalo, Franco Grisafi, and Giorgio Micale. Numerical prediction of flow fields in baffled stirred vessels: A comparison of alternative modelling approaches. *Chemical Engineering Science*, 53(21):3653–3684, 1998.

[24] Francois Cabaret, Louis Fradette, and Philippe A. Tanguy. New tur-

bine impellers for viscous mixing. *Chemical Engineering & Technology: Industrial Chemistry-Plant Equipment-Process Engineering-Biotechnology*, 31(12):1806–1815, 2008.

[25] Choe Earn Choong, Shaliza Ibrahim, and Ahmed El-Shafie. Artificial Neural Network (ANN) model development for predicting just suspension speed in solid-liquid mixing system. *Flow Measurement and Instrumentation*, page 101689, 2020.

[26] Clayton T. Crowe, John D. Schwarzkopf, Martin Sommerfeld, Yutaka Tsuji, John D. Schwarzkopf, Martin Sommerfeld, and Yutaka Tsuji. *Multiphase Flows with Droplets and Particles*. CRC Press, August 2011.

[27] J. de la Villéon, F. Bertrand, P. A. Tanguy, R. Labrie, J. Bousquet, and D. Lebouvier. Numerical investigation of mixing efficiency of helical ribbons. *AIChE Journal*, 44(4):972–977, 1998.

[28] Bastien Delacroix, Anya Bouarab, Louis Fradette, François Bertrand, and Bruno Blais. Simulation of granular flow in a rotating frame of reference using the discrete element method. *Powder Technology*, 369:146–161, 2020.

[29] J. J. Derksen. Highly resolved simulations of solids suspension in a small mixing tank. *AIChE Journal*, 58(10):3266–3278, 2012.

[30] R. Di Felice. The voidage function for fluid-particle interaction systems. *International Journal of Multiphase Flow*, 20(1):153–159, 1994.

[31] W. D. Einenkel and A. Mersmann. The agitator speed for particle suspension. *Verfahrenstehnik*, 11:90, 1977.

[32] E. A. Fadlun, R. Verzicco, Paolo Orlandi, and J. Mohd-Yusof. Combined immersed-boundary finite-difference methods for three-dimensional complex flow simulations. *Journal of computational physics*, 161(1):35–60, 2000.

[33] David F. Fletcher and Gary J. Brown. Numerical simulation of solid suspension via mechanical agitation: Effect of the modelling approach, turbulence model and hindered settling drag law. *International Journal of Computational Fluid Dynamics*, 23(2):173–187, 2009.

[34] Dimitri Gidaspow. *Multiphase Flow and Fluidization: Continuum and Kinetic Theory Descriptions*. Academic press, 1994.

[35] J. C. Godfrey and Z. M. Zhu. Measurement of particle-liquid profiles in agitated tanks. In *AIChE Symposium Series*, volume 90, pages 181–185. New York, NY: American Institute of Chemical Engineers, 1971-c2002., 1994.

[36] R.K. Grenville, J.J. Giacomelli, and D.A.R. Brown. Suspension of solid particles in vessels agitated by Rushton turbine imperllers. *Chemical Engineering Research and Design*, 109:730–733, 2016.

[37] Deyin Gu, Zuohua Liu, Facheng Qiu, Jun Li, Changyuan Tao, and Yundong Wang. Design of impeller blades for efficient homogeneity of solid-liquid suspension in a stirred tank reactor. *Advanced Powder Technology*, 28(10):2514–2523, 2017.

[38] S. Ibrahim and A.W. Nienow. Comparing Impeller Performance for Solid-Suspension in the Transitional Flow Regime with Newtonian Fluids. *Chemical Engineering Research and Design*, 77(8):721–727, 1999.

[39] Raad I. Issa. Solution of the implicitly discretised fluid flow equations by operator-splitting. *Journal of computational physics*, 62(1):40–65, 1986.

[40] K. L. JOHNSON. Normal contact of elastic solids : Hertz theory. *Contact Mechanics*, pages 84–106, 1989.

[41] G. R. Kasat, A. R. Khopkar, V. V. Ranade, and A. B. Pandit. CFD simulation of liquid-phase mixing in solid–liquid stirred reactor. *Chemical Engineering Science*, 63(15):3877–3885, 2008.

[42] F. Kneule. Die prüfung von rührern durch löslichkeitsbestimmung. *Chemie Ingenieur Technik*, 28(3):221–225, 1956.

[43] Irvin M. Krieger and Thomas J. Dougherty. A mechanism for non-Newtonian flow in suspensions of rigid spheres. *Transactions of the Society of Rheology*, 3(1):137–152, 1959.

[44] Basak Kutukcu and Inci Ayranci. Application of pressure gauge measurement method beyond its limits. *Chemical Engineering Research and Design*, 141:170–180, 2019.

[45] Manon Lassaigne, Bruno Blais, Louis Fradette, and François Bertrand. Experimental investigation of the mixing of viscous liquids and non-dilute concentrations of particles in a stirred tank. *Chemical Engineering Research and Design*, 108:55–68, April 2016.

[46] Mattias Ljungqvist and Anders Rasmuson. Numerical simulation of the two-phase flow in an axially stirred vessel. *Chemical Engineering Research and Design*, 79(5):533–546, 2001.

[47] J. Y. Luo and A. D. Gosman. Prediction of impeller-induced flow in mixing vessels using multiple frames of reference. INSTITUTE OF CHEMICAL ENGINEERS SYMPOSIUM SERIES, 1994.

[48] G. Micale, F. Grisafi, and A. Brucato. Assessment of Particle Suspension Conditions in Stirred Vessels by Means of Pressure Gauge Technique. *Chemical Engineering Research and Design*, 80(8):893–902, 2002.

[49] G. Micale, F. Grisafi, L. Rizzuti, and A. Brucato. CFD simulation of particle suspension height in stirred vessels. *Chemical Engineering Research and Design*, 82(9):1204–1213, 2004.

[50] R. D. MINDLIN. Elastic Spheres in Contact Under Varying Oblique Forces. *J. Applied Mech.*, 20:327–344, 1953.

[51] Prakash Mishra and Farhad Ein-Mozaffari. Critical review of different aspects of liquid-solid mixing operations. *Reviews in Chemical Engineering*, 0(0), 2019.

[52] G. Montante, K.C. Lee, A. Brucato, and M. Yianneskis. Numerical simulations of the dependency of flow pattern on impeller clearance in stirred vessels. *Chemical Engineering Science*, 56(12):3751–3770, 2001.

[53] M. Moštěk, A. Kukukova, M. Jahoda, and V. Machoň. Comparison of different techniques for modelling of flow field and homogenization in stirred vessels. *Chemical Papers*, 59(6a):380–385, 2005.

[54] A.W. Nienow. Suspension of solid particles in turbine agitated baffled vessels. *Chemical Engineering Science*, 23(12):1453–1459, 1968.

[55] Hamid Reza Norouzi, Reza Zarghami, Rahmat Sotudeh-Gharebagh, and Navid Mostoufi. *Coupled CFD-DEM Modeling: Formulation, Implementation and Application to Multiphase Flows*. John Wiley & Sons, 2016.

[56] J. Y. Oldshue and R. N. Sharma. The Effect of Off-Bottom Distance of an Impellar for the" Just Suspended Speed" N~ j~ s. In *AIChE Symposium Series*, volume 88, pages 72–72. American Institute of Chemical Engineers, 1992.

[57] Edward L. Paul, Victor A. Atiemo-Obeng, and Suzanne M. Kresta. *Handbook of Industrial Mixing: Science and Practice*. John Wiley & Sons, February 2004.

[58] Charles S. Peskin. Flow patterns around heart valves: A numerical method. *Journal of computational physics*, 10(2):252–271, 1972.

[59] Charles S. Peskin. The immersed boundary method. *Acta numerica*, 11:479–517, 2002.

[60] S. Pirker, D. Kahrimanovic, and C. Goniva. Improving the applicability of

discrete phase simulations by smoothening their exchange fields. *Applied Mathematical Modelling*, 35(5):2479–2488, 2011.

[61] Aravind R. Rammohan, Milorad P. Duduković, and Vivek V. Ranade. Eulerian flow field estimation from particle trajectories: Numerical experiments for stirred tank type flows. *Industrial & engineering chemistry research*, 42(12):2589–2601, 2003.

[62] Vilas B. Rewatkar, KSMS Raghava Rao, and Jyeshtharaj B. Joshi. Critical impeller speed for solid suspension in mechanically agitated three-phase reactors. 1. Experimental part. *Industrial & Engineering Chemistry Research*, 30(8):1770–1784, 1991.

[63] L. W. Rong, K. J. Dong, and A. B. Yu. Lattice-Boltzmann simulation of fluid flow through packed beds of uniform spheres: Effect of porosity. *Chemical Engineering Science*, 99:44–58, 2013.

[64] Sushil S. Shirsath, J. T. Padding, J. a. M. Kuipers, Tim W. J. Peeters, and H. J. H. Clercx. Numerical Investigation of Monodisperse Granular Flow Through an Inclined Rotating Chute. *AIChE Journal*, 60(10):3424–3441, October 2014.

[65] Sushil S. Shirsath, Johan T. Padding, J. A. M. (Hans) Kuipers, and Her-

man J. H. Clercx. Simulation study of the effect of wall roughness on the dynamics of granular flows in rotating semicylindrical chutes. *AIChE Journal*, 61(7):2117–2135, July 2015.

[66] A. Tamburini, A. Brucato, A. Busciglio, A. Cipollina, F. Grisafi, G. Micale, F. Scargiali, and G. Vella. Solid-Liquid Suspensions in Top-Covered Unbaffled Vessels: Influence of Particle Size, Liquid Viscosity, Impeller Size, and Clearance. *Ind. Eng. Chem. Res.*, 53(23):9587–9599, June 2014.

[67] A. Tamburini, A. Brucato, A. Cipollina, G. Micale, and M. Ciofalo. CFD predictions of sufficient suspension conditions in solid-liquid agitated tanks. *International Journal of Nonlinear Sciences and Numerical Simulation*, 13(6):427–443, 2012.

[68] A. Tamburini, A. Cipollina, G. Micale, A. Brucato, and M. Ciofalo. CFD simulations of dense solid–liquid suspensions in baffled stirred tanks: Prediction of suspension curves. *Chemical Engineering Journal*, 178:324–341, 2011.

[69] A. Tamburini, A. Cipollina, G. Micale, A. Brucato, and M. Ciofalo. CFD simulations of dense solid–liquid suspensions in baffled stirred tanks: Pre-

diction of the minimum impeller speed for complete suspension. *Chemical engineering journal*, 193:234–255, 2012.

[70] A. Tamburini, A. Cipollina, G. Micale, A. Brucato, and M. Ciofalo. CFD simulations of dense solid–liquid suspensions in baffled stirred tanks: Prediction of solid particle distribution. *Chemical engineering journal*, 223:875–890, 2013.

[71] A. Tamburini, A. Cipollina, G. Micale, A. Brucato, and M. Ciofalo. Influence of drag and turbulence modelling on CFD predictions of solid liquid suspensions in stirred vessels. *Chemical Engineering Research and Design*, 92(6):1045–1063, 2014.

[72] Alessandro Tamburini, Andrea Cipollina Giorgio Micale, and Italy Palermo. CFD Simulation of Solid Liquid Suspensions in Baffled Stirred Vessels Below Complete Suspension Speed. *Chemical Engineering Transactions*, 2011.

[73] Gary B. Tatterson. *Fluid Mixing and Gas Dispersion in Agitated Tanks*. McGraw-Hill New York, 1991.

[74] SHAO Ting, H. U. Yinyu, WANG Wentan, J. I. N. Yong, and Yi CHENG. Simulation of solid suspension in a stirred tank using CFD-DEM coupled

approach. *Chinese Journal of Chemical Engineering*, 21(10):1069–1081, 2013.

[75] Y. Tsuji, T. Tanaka, and T. Ishida. Lagrangian numerical simulation of plug flow of cohesionless particles in a horizontal pipe. *Powder Technology*, 71(3):239–250, September 1992.

[76] Yutaka Tsuji. Multi-scale modeling of dense phase gas–particle flow. *Chemical Engineering Science*, 62(13):3410–3418, 2007.

[77] Z. Y. Zhou, S. B. Kuang, K. W. Chu, and A. B. Yu. Discrete particle simulation of particle–fluid flow: Model formulations and their applicability. *Journal of Fluid Mechanics*, 661:482–510, 2010.

[78] H. P. Zhu, Z. Y. Zhou, R. Y. Yang, and A. B. Yu. Discrete particle simulation of particulate systems: Theoretical developments. *Chemical Engineering Science*, 62(13):3378–3396, July 2007.

[79] H. P. Zhu, Z. Y. Zhou, R. Y. Yang, and A. B. Yu. Discrete particle simulation of particulate systems: A review of major applications and findings. *Chemical Engineering Science*, 63(23):5728–5770, December 2008.

[80] Th. N. Zwietering. Suspending of solid particles in liquid by agitators. *Chemical Engineering Science*, 8(3):244–253, June 1958.